J|A|C|S
ARTICLES
Published on Web 03/17/2007

The Catalytic Mn^{2+} Sites in the Enolase−Inhibitor Complex: Crystallography, Single-Crystal EPR, and DFT Calculations

Raanan Carmieli,[†] Todd M. Larsen,[‡] George H. Reed,[‡] Samir Zein,[#] Frank Neese,[#] and Daniella Goldfarb*,[†]

Contribution from the Departments of Chemical Physics, The Weizmann Institute of Science, Rehovot, Israel 76100, Department of Biochemistry, University of Wisconsin, Madison, Wisconsin 53726-4087, and Institute of Physical Chemistry and Theoretical Chemistry, University of Bonn, Wegelerstr. 12, D-53115 Bonn, Germany

Received August 30, 2006; E-mail: daniella.goldfarb@weizmann.ac.il

Abstract: Crystals of Zn^{2+}/Mn^{2+} yeast enolase with the inhibitor PhAH (phosphonoacetohydroxamate) were grown under conditions with a slight preference for binding of Zn^{2+} at the higher affinity site, site I. The structure of the Zn^{2+}/Mn^{2+}−PhAH complex was solved at a resolution of 1.54 Å, and the two catalytic metal binding sites, I and II, show only subtle displacement compared to that of the corresponding complex with the native Mg^{2+} ions. Low-temperature echo-detected high-field (W-band, 95 GHz) EPR (electron paramagnetic resonance) and ^{1}H ENDOR (electron−nuclear double resonance) were carried out on a single crystal, and rotation patterns were acquired in two perpendicular planes. Analysis of the rotation patterns resolved a total of six Mn^{2+} sites, four symmetry-related sites of one type and two out of the four of the other type. The observation of two chemically inequivalent Mn^{2+} sites shows that Mn^{2+} ions populate both sites I and II and the zero-field splitting (ZFS) tensors of the Mn^{2+} in the two sites were determined. The Mn^{2+} site with the larger *D* value was assigned to site I based on the ^{1}H ENDOR spectra, which identified the relevant water ligands. This assignment is consistent with the seemingly larger deviation of site I from octahedral symmetry, compared to that of site II. The ENDOR results gave the coordinates of the protons of two water ligands, and adding them to the crystal structure revealed their involvement in a network of H bonds stabilizing the binding of the metal ions and PhAH. Although specific hyperfine interactions with the inhibitor were not determined, the spectroscopic properties of the Mn^{2+} in the two sites were consistent with the crystal structure. Density functional theory (DFT) calculations carried out on a cluster representing the catalytic site, with Mn^{2+} in site I and Zn^{2+} in site II, and vice versa, gave overestimated *D* values on the order of the experimental ones, although the larger *D* value was found for Mn^{2+} in site II rather than in site I. This discrepancy was attributed to the high sensitivity of the ZFS parameters to the Mn−O bond lengths and orientations, such that small, but significant, differences between the optimized and crystal structures alter the ZFS considerably, well above the difference between the two sites.

Introduction

Electron paramagnetic resonance (EPR) and electron−nuclear double resonance (ENDOR) experiments carried out at high fields/high frequencies facilitate measurements of single crystals of metalloproteins due to the considerable increase in sensitivity for size-limited samples as compared to conventional X-band (∼9.5 GHz, 0.35 T) measurements.[1−5] This is particularly true for Mn^{2+} ($S = 5/2$)- containing proteins because of the reduced intensity of forbidden transitions which leads to increased resolution and sensitivity. EPR/ENDOR single-crystal measurements, focusing on the metal binding site, provide the following complementary information to X-ray crystallography: (i) insight into the electronic structure and bonding characteristic; (ii) direct detection of proton locations at the binding site (most relevant for water or OH groups, which may play an important role in the enzyme mechanism); (iii) allow comparing structures in solution and crystals; and finally, (iv) in the specific case of Mn^{2+}, to provide the relation between the zero-field splitting (ZFS) tensor and the atomic coordinates. This can then be used as a reference when attempting to derive structural information from ZFS tensor components in systems with unknown structures. The Mn^{2+} coordination environment in proteins differs significantly from that found in Mn^{2+} doped inorganic crystals, the complete ZFS tensor of which has been determined. Therefore, such crystals are not appropriate models for metal binding sites in proteins. Hence, the availability

[†] The Weizmann Institute of Science.
[‡] University of Wisconsin.
[#] University of Bonn.

(1) Coremans, J. W. A.; Poluektov, O. G.; Groenen, E. J. J.; Canters, G. W.; Nar, H.; Messerschmidt, A. *J. Am. Chem. Soc.* **1994**, *116*, 3097−3101.
(2) Manikandan, P.; Carmieli, R.; Shane, T.; Kalb (Gilboa), A. J.; Goldfarb, D. *J. Am. Chem. Soc.* **2000**, *122*, 3488−3494.
(3) Carmieli, R.; Manikandan, P.; Kalb, A. J.; Goldfarb, D. *J. Am. Chem. Soc.* **2001**, *123*, 8378−8386.
(4) Carmieli, R.; Manikandan, P.; Epel, B.; Kalb (Gilboa), A. J.; Schnegg, A.; Savitsky, A.; Mobius, K.; Goldfarb, D. *Biochemistry* **2003**, *42*, 7863−7870.
(5) Hogbom, M.; Galander, M.; Andersson, M.; Kolberg, M.; Hofbauer, W.; Lassmann, G.; Nordlund, P.; Lendzian, F. *Proc. Natl. Acad. Sci. U.S.A.* **2003**, *100*, 3209−3214.

 10.1021/ja066124e CCC: $37.00

of the ZFS tensor for Mn^{2+} binding sites in proteins can serve as a reference for unknown structures as well as for theoretical/computational investigations designed to predict local structure based on the ZFS parameters.

While considerable attention has been devoted to relations between the *g* and hyperfine tensors and structural properties using DFT calculations,[6] the ZFS has not yet attracted enough attention from the theoretical community, perhaps because it is an extremely complicated property to calculate from first physical principles. The detailed treatment shows that it contains second-order spin−orbit coupling contributions from excited states of the same multiplicities as those of the ground states as well as from spin flips.[7] Second, the ZFS contains a direct dipolar spin−spin coupling contribution that is of two-electron nature.[8] While it has been previously thought that the spin−spin coupling is negligible in transition-metal complexes, recent evidence suggests that this is not the case.[9] Because the task to accurately calculate spin-dependent two-electron second-order properties is extremely complex, until recently there has been no quantum chemical program that calculates all parts of the ZFS from first principles. This has only changed most recently,[9,10] where it became clear that the ZFS is well-predicted by correlated ab initio methods, which are clearly superior to DFT-based calculations. However, the former are too computationally demanding to be applied to molecules of the size studied here, and consequently, one has to resort to DFT methods for practical reasons. Still, due to the recent developments, it is now possible to start addressing the reliability of such calculations for actual systems of interest. So far, preliminary results indicate that the DFT methods used are of moderate accuracy with errors being typically within a factor of 2, while the experimental trends are usually well-reproduced for series of related compounds.[9−14]

Our earlier work, demonstrating the feasibility of high-field EPR/ENDOR single-crystal studies of Mn^{2+} in proteins,[2−4] was carried out on concanavalin A, where the Mn^{2+} plays a structural role.[15] In this protein, the Mn^{2+} has a relatively small ZFS, and the crystal has an orthorhombic unit cell with coinciding morphological and crystallographic planes. In these measurements, we found that, while the crystal structure determined by X-ray crystallography at low temperature (77 K) reported only one type of Mn^{2+},[16] the spectroscopic measurements, also carried out at low temperatures, clearly distinguished two types of Mn^{2+}, having different ZFS tensors. Interestingly, the two sites were found to undergo a two-site exchange, with complete

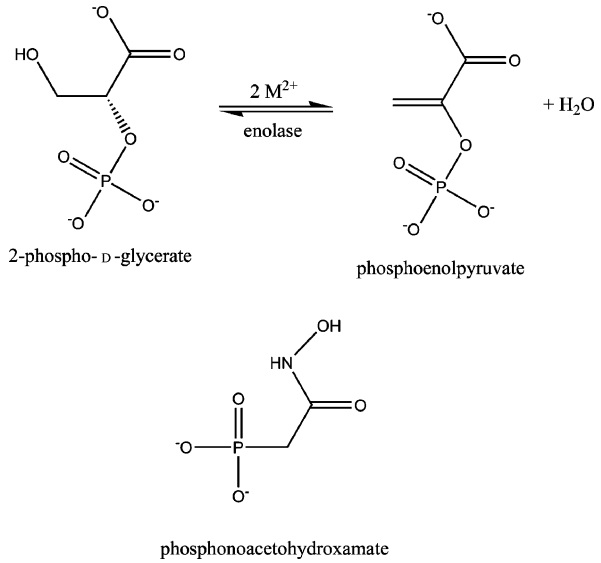

Figure 1. The enolase dehydration reaction and the structure of the inhibitor PhAH.

averaging at room temperature in the crystalline state, which was not detected by the crystallography measurements.

In the present work, the catalytic, divalent cation binding sites in yeast enolase were examined. Enolase catalyzes the reversible dehydration of D-2-phosphoglycerate (2PGA) to phosphoenolpyruvate (PEP) (Figure 1) as a step in glycolysis,[17] and it requires two equivalents of divalent cations for activity.[18] The in vivo requirement is satisfied by Mg^{2+}, but other ions such as Mn^{2+} and Zn^{2+} are active in vitro.[19] The complex of the enzyme with the potent inhibitor, PhAH (phosphonoacetohydroxamate), was examined because, in this complex, there is at least a preference for formation of hybrid Zn^{2+}/Mn^{2+} complexes as opposed to spin-coupled Mn^{2+}/Mn^{2+} complexes.[20] PhAH is a slow, tight binding inhibitor of enolase having a K_i of 15 pM.[21] The structure of the bis Mg^{2+}−PhAH complex of enolase shows that the inhibitor forms a bis-chelate complex in which the carbonyl oxygen of the inhibitor bridges the two Mg^{2+} ions.[22] This bis-chelate coordination scheme carries over to complexes of Mg^{2+} with the substrates 2PGA and PEP.[23] Enolase carries out the interconversion of 2PGA and PEP in a stepwise manner[24] that enlists general acid−base catalysis from Lys345 and Glu211.[25,26] The enolate intermediate, generated by removal of a proton from C2 of 2PGA, is stabilized by the two equivalents of divalent cation and by the protonated ϵ amino group of Lys396.[23,26] The in vitro activity of the Mn^{2+} enolase allowed extensive EPR spectroscopic investigations of the

(6) Kaupp, M., Bühl, M., Malkin, V., Eds. *Calculation of NMR and EPR Parameters. Theory and Applications*; Wiley-VCH: New York, 2004.
(7) Neese, F.; Solomon, E. I. *Inorg. Chem.* **1998**, *37*, 6568−6582.
(8) Neese, F. Zero-Field Splitting. In *Calculation of NMR and EPR Parameters. Theory and Applications*; Kaupp, M., Bühl, M., Malkin, V., Eds.; Wiley-VCH: New York, 2004; pp 541−564.
(9) Neese, F. *J. Am. Chem. Soc.* **2006**, *128*, 10213−1022.
(10) Ganyushin, D.; Neese, F. *J. Chem. Phys.* **2006**, *125*, 024103-1−024103-11.
(11) Schöneboom, J.; Neese, F.; Thiel, W. *J. Am. Chem. Soc*. **2005**, *127*, 5840−5853.
(12) Neese, F. *J. Inorg. Biochem*. **2006**, *100*, 716−726. Special issue on high-valent Fe(IV).
(13) Ray, K.; Begum, A; Weyhermüller, T.; Piligkos, S.; van Slageren, J.; Neese, F.; Wieghardt, K. *J. Am. Chem. Soc*. **2005**, *127*, 4403−4415.
(14) Sinnecker, S.; Neese, F. *J. Phys. Chem. A* **2006**, *110*, 12267−12275.
(15) Kalb (Gilboa), A. J.; Habash, J.; Hunter, N. S.; Price, H. J.; Raftery, J.; Helliwell, J. R. In *Metal Ions in Biological Systems*; Sigel, A., Sigel, H., Eds.; Marcel Dekker Inc.: New York, 2000; Vol. 37.
(16) Deacon, A.; Gleichmann, T.; Kalb (Gilboa), A. J. *J. Chem. Soc., Dalton Trans.* **1997**, *93*, 4305−4312.
(17) Lohman, K.; Meyerhof, O. *Biochem. Z.* **1934**, *273*, 60−72.
(18) Faller, L. D.; Baroudy, B. M.; Johnson, A. M.; Ewall, R. X. *Biochemistry* **1977**, *16*, 3864−3869.
(19) Poyner, R. R.; Cleland, W. W.; Reed, G. H. *Biochemistry* **2001**, *40*, 8009−8017.
(20) Poyner, R. R.; Reed, G. H. *Biochemistry* **1992**, *31*, 7166−7173.
(21) Anderson, V. E.; Weiss, P. M.; Cleland, W. W. *Biochemistry* **1984**, *23*, 2779−2786.
(22) Wedekind, J. E.; Poyner, R. R.; Reed, G. H.; Rayment, I. *Biochemistry* **1994**, *33*, 9333−9342.
(23) Larsen, T. M.; Wedekind, J. E.; Rayment, I.; Reed, G. H. *Biochemistry* **1996**, *35*, 4349−4358.
(24) Dinovo, E. C.; Boyer, P. D. *J. Biol. Chem.* **1971**, *246*, 4586−4593.
(25) Poyner, R. R.; Laughlin, L. T.; Sowa, G. A.; Reed, G. H. *Biochemistry* **1996**, *35*, 1692−1699.
(26) Reed, G. H.; Poyner, R. R.; Larsen, T. M.; Wedekind, J. E.; Rayment, I. *Curr. Opin. Struct. Biol*. **1996**, *6*, 736−743.

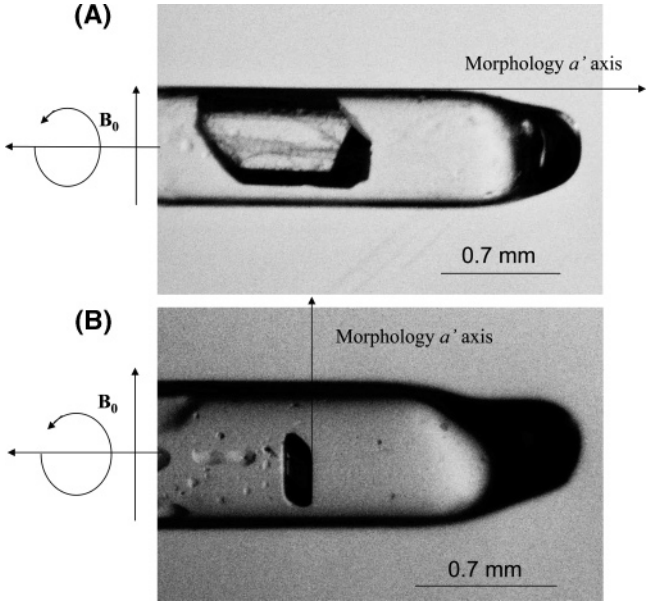

Figure 2. The orientation of the enolase crystals in the EPR tube and the definition of the morphology axis. (A) The crystal mounted with the a' axis parallel to the tube axis. (B) The crystal mounted with the a' axis perpendicular to the tube axis. The rotation axis is shown as well.

enolase reaction mechanism in solution, revealing the proximity of the metal ions and providing further insight into the structure of the metal binding site and the reaction mechanism.[20]

Here, we present a detailed characterization of the Mn^{2+} binding sites in crystals of the enolase (Zn^{2+}/Mn^{2+})−PhAH complex using crystallography and single-crystal high-field (W-band, 95 GHz) EPR and ENDOR measurements. These provided the structure and the ZFS tensors of the Mn^{2+} in sites I and II and the coordinates of the protons of two water ligands, which were found to be involved in a hydrogen-bonding network, stabilizing the binding of the metal ions and PhAH. These results provide an excellent opportunity and a test case for the application of DFT methods, based on recent advances in calculating ZFS tensors to account for their size and orientation.

Experimental Section

A. Crystallization, Data Collection, and Refinement. Crystals were grown at room temperature by the batch method from 10 mg/mL of protein, 0.25 M KCl, 0.43 mM $MnCl_2$, 0.43 mM $ZnCl_2$, 2 mM PhAH, 13% PEG 8000, and 30 mM HEPES/KOH (pH 7.0). The setup was microseeded with crystals of wild-type enolase complexed with substrate and Mn^{2+}. An equivalent of Zn^{2+} was added first, expecting to populate primarily site I, and the subsequent addition of a second equivalent of Mn^{2+} was expected to be mainly in site II. Crystals of various sizes grew within 1 day.

The X-ray data were collected on a single crystal. A single crystal of the variant was transferred into a solution (solution A) that contained 50 mM HEPES (pH 7.0), 20% PEG 8000, 0.3 M KCl, 0.43 mM $MnCl_2$, 0.43 mM $ZnCl_2$, and 2 mM PEP. The crystal was allowed to equilibrate in solution A for 20 s prior to a five-step serial transfer into solutions that contained increasing concentrations (4% per step) of the cryoprotectant ethylene glycol. An equilibration time of 5 s between each of the successive steps was used throughout the serial transfers. After the last serial transfer, the crystal was flash-frozen and stored in liquid nitrogen. The same procedure was used for the crystals used in the EPR/ENDOR measurements.

Table 1. Summary of the Crystallographic Data of the Enolase Zn^{2+}/Mn^{2+}−PhAH Complex

space group	$P2_1$
cell dim. (Å) *a*, *b*, *c*	72, 65.1, 85.9
β angle	99.5°
no. of measurements	399256
no. of independent reflections	115031
data range (Å)	30−1.54
completeness (%)	
overall	99.4
last shell	98.7 (1.60−1.54)
R merge (%)	
overall	3.8
last shell	14.7
refinement statistics	
R cryst. (%)	15.8
R factor (free) 5% data (%)	17.9
rmsd of bonds (Å)	0.008
rmsd of angles (deg)	1.1
no. of water molecules	889

X-ray data were collected at 100 K on a 3 × 3 mosaic CCD detector[27,28] at the Structural Biology Center 19−BM Beamline (Advanced Photon Source, Argonne National Laboratory). The program HKL2000[29] was used for crystallographic data integration and reduction. Initial phases were calculated from the refined coordinates of wild-type enolase−Mg^{2+} complex (PDB 2AL1)[30] minus the substrate, Mg^{2+} ions, and the water molecules. Refinement was performed using REFMAC from the CCP4 package.[31] Observation of the structure with the graphics program TURBO[32] revealed that the following residues required adjustments: residues 154−167 and 251−278 in subunit 1 and residues 157−167 and 259−271 in subunit 2. These residues were removed, REFMAC refinement was performed, and the resulting F_o-F_c density maps were used to rebuild the removed residues. Residues 158−162 in subunit 1 and residues 159−161 in subunit 2 were disordered and, therefore, were not included in the model. Densities corresponding to residues 263 − 271 in subunit 1 and 268−271 in subunit 2 were weak for several side chains; however, all residues were definable and included in the model. Density corresponding to PhAH and the metal ions was clearly present in both subunits. After inclusion of PhAH and the metal ions, water molecules were included in the model. Further adjustments to the model were made using TURBO followed by refinement with REFMAC. Refinement statistics are given in Table 1. Site I was arbitrarily assigned as Zn^{2+} and site II as Mn^{2+} for refinement. The final PDB has the symbol M^{2+} in all metal sites representing either Mn^{2+} or Zn^{2+}. The programs BOBSCRIPT[33] and MOLSCRIPT[34] were used to prepare Figures 4, 5, and 6. Weblab ViewerLite was used for Figures 9 and 12.

1. Spectroscopic Measurements. The crystals were mounted, with the aid of a polarizing microscope, into 0.7 mm o.d. thin-walled quartz tubes. The crystals used had an average size of 0.3 × 0.4 × 0.3 mm^3 and a well-defined morphology, as shown in Figure 2, with a long axis defined as a'. Measurements were carried out on several crystals in two perpendicular planes, one with a' parallel to the tube axis and the other with a' perpendicular to it. The rotation patterns were acquired by rotating the tube, the axis of which is perpendicular to the magnetic field direction. BDPA (α,γ-bisdiphenylene-β-phenylallyl) dissolved in a polyethylene film and glued to one of the cavity flanges was used as

(27) Gao, Y. G.; Robinson, H.; Sanishvili, R.; Joachimiak, A.; Wang, A. H. *Biochemistry* **1999**, *38*, 16452−16460.
(28) Walsh, M. A.; Dementieva, I.; Evans, G.; Sanishvili, R.; Joachimiak, A. *Acta Crystallogr., Sect. D* **1999**, *55*, 1168−1173.
(29) Otwinowski, Z.; Minor, W. *Methods Enzymol.* **1997**, *276*, 307−326.
(30) Sims, P. A.; Menefee, A. L.; Larsen, T. M.; Mansoorabadi, S. O.; Reed, G. H. *J. Mol. Biol.* **2006**, *355*, 422−431.
(31) Winn, M. D.; Isupov, M. N.; Murshudov, G. N. *Acta Crystallogr., Sect. D* **2001**, *57*, 122−133.
(32) Roussel, A.; Cambillau, C. *Silicon Graphics Geometry Partners Directory*; Silicon Graphics: Mountain View, CA, 1991.
(33) Esnouf, R. M. *Acta Crystallogr., Sect. D* **1999**, *55*, 938−940.
(34) Kraulis, P. J. *J. Appl. Crystallogr.* **1991**, *24*, 946−950.

an internal standard for the alignment of the EPR spectra. The magnetic field was determined from the ^{1}H Larmor frequency obtained from the ^{1}H ENDOR spectra. All EPR/ENDOR experiments were carried out on a W-band (95 GHz, ~3.5 T) home-built spectrometer described earlier.[35] Continuous-wave (CW) EPR spectra were collected at room temperature and at 5 K with a modulation frequency of 100 kHz and an amplitude of 0.2 mT.

Pulsed EPR and ENDOR experiments were carried out at 4.5 ± 0.1 K. Field sweep−echo-detected (FS−ED) EPR spectra were obtained using the two-pulse echo sequence ($(\pi/2) - \tau - \pi - \tau -$ echo), where the echo intensity was measured as a function of the magnetic field with microwave (MW) pulse lengths (t_{MW}) of 0.03 and 0.06 μs and τ = 0.35 μs. The ^{1}H ENDOR spectra were measured with the Davies ENDOR pulse sequence ($\pi - T - (\pi/2) - \tau - \pi - \tau -$ echo, with a RF pulse applied during the time T) and t_{MW} = 0.2, 0.1, and 0.2 μs, τ = 0.4 μs, t_{RF} = 25 μs, and T = 30 μs. The frequency scale of the ENDOR spectra is given with respect to the ^{1}H Larmor frequency, $\nu = \nu_{RF} - \nu_H$. EPR spectra were recorded from 0 to 180° every 5°, and ENDOR spectra were recorded every 10°. Several crystals were used such that the rotation patterns were collected more than once to ensure reproducibility.

2. Simulations and Data Analysis. When the ZFS parameter D is small with respect to the Zeeman interaction, $g\beta B_0$, second-order perturbation theory yields the following resonant magnetic fields for the $|-1/2, m\rangle \rightarrow |1/2, m\rangle$ EPR transitions[36]

$$B\left(\frac{1}{2}, m\right) = B_0 - \left[\frac{mA}{g\beta}\right] + f(D,E,\theta,\phi) - mF \quad (1)$$

where

$$f(D,E,\theta,\phi) = \frac{16}{g\beta B_0}\Big\{(D - E\cos 2\phi)^2 \sin^2\theta \cos^2\theta + E^2 \sin^2 2\phi \sin^2\theta - \frac{1}{8}[D\sin^2\theta + E\cos 2\phi(1+\cos^2\theta)]^2 - \frac{1}{2}E^2\cos^2\theta\sin^2 2\phi\Big\} \quad (2)$$

and m is the ^{55}Mn nuclear spin state, A is the ^{55}Mn isotropic hyperfine coupling constant, F includes cross-terms between the ZFS and the hyperfine interaction of the order of $AD^2/(g\beta B_0)^2$. D and E are related to the principal components of the ZFS tensor, **D**, as follows: $D = (3/2)D_{zz}$ and $E = (1/2)(D_{yy} - D_{xx})$. The angles θ and ϕ give the orientation of the magnetic field with respect to the principal axis system of **D**. When working with single crystals, it is convenient to express θ and ϕ in terms of several reference frames. In this work, we have used the following frames: the principal axis system of the magnetic tensor, $P(x,y,z)$, the morphology frame of reference, $M(c',b',a')$, the sample tube frame, $T(x',y',z')$, where z' is along the tube axis, the goniometer frame $G(x'',y'',z'')$, and the lab frame $B(X,Y,Z)$, where $Z \parallel \vec{B}_0$. Normally, when the orientation of the crystallographic axes relative to crystal morphology are known, the M frame is replaced with the crystallographic reference frame. However, in our case, this was not known a priori, and we were unable to determine it due to technical difficulties we encountered with the X-ray measurements. Therefore, we replaced it with the well-defined morphology reference frame. The relation between the crystal and morphology frames was determined from the EPR results using the symmetry properties of the crystals, as described in the Supporting Information. The transformation between the various frames is done using the appropriate Euler angles and the corresponding Wigner rotation matrices, **R**. For our experimental setup, the transformations are

$$P \xrightarrow{\alpha,\beta,\gamma} M \xrightarrow{\phi',\theta',\psi} T \xrightarrow{0,0,\varphi_0} G \xrightarrow{\phi_t,90°,0} B \quad (3)$$

The rotation patterns were acquired by measuring the spectrum as a function of the rotation angle of the goniometer, ϕ_t. The relation between the above sets of angles and θ and ϕ used in eq 4 is

$$R(-\phi, -\theta, 0) = R(\phi_t, 90°, \theta)R(0,0,\varphi_0)R(\phi',\theta',\psi)R(\alpha,\beta,\gamma) \quad (4)$$

All angles in eq 4, except α, β, and γ, are defined by the experimental conditions.

Because the crystals were not aligned along crystallographic planes, φ_0 could not be easily determined from symmetry behavior of the rotation patterns but rather had to be determined from the best-fit analysis. The fit was carried out by finding a relative φ_0 value for which the rotation pattern of both planes (setting arbitrarily $\varphi_0 = 0$ for one plane) could be fitted with reasonable and close values of A, D, and E/D. Once φ_0 was found, A, D, and E/D were fixed for all four symmetry-related Mn^{2+} ions belonging to the same type, and the procedure continued by varying only α, β, and γ.

Because the enolase EPR spectra were rather complicated, with limited resolution due to the large number of sites, the identification of individual rotation patterns was much more complicated than in our previous study of concanavalin A;[4] therefore, a more sophisticated search had to be applied. For this purpose, a MATLAB program that can fit Mn^{2+} EPR rotation patterns (based on eq 1) was developed. In this program, the user can select only a part of the rotation pattern, and the program finds all possible trajectories and reports those with the lowest least-square errors.[37] Initially, the fitting procedure was applied to each plane individually. Once two full trajectories having close parameters were found in both planes, these two trajectories were chosen, and the fit was further refined by fitting them simultaneously.

The fitting of the data gave **D** in the morphology axis system. In order to relate it to molecular quantities, the relationship between the morphological axes and the crystallographic axes, given by α',β',γ', had to be determined. These angles were obtained using the symmetry properties of the crystals (see Supporting Information for details).

The analysis of the ENDOR spectra was similar to the EPR analysis; it was first carried out with respect to the morphology axes, and then, the transformation to the crystallographic axes, found from the EPR analysis, was applied. The fitting program is, in general, similar to that of the EPR program, and it yields the best-fit hyperfine tensor **A**. Its principal values are A_{xx}, A_{yy}, and A_{zz}, and they are further expressed in terms of an isotropic, a_{iso}, and anisotropic part, **T**. On the basis of our earlier concanavalin A results,[4] **T** was taken as axial, and the point-dipole approximation was applied such that

$$T_\perp = \frac{\mu_0}{4\pi}\frac{gg_n\beta\beta_n}{r^3} \quad (5)$$

where r is the Mn−H distance and the other symbols have their usual meaning. At W-band, the ^{1}H ENDOR frequencies of the $M_S = \pm 1/2$ manifolds can be described by the first-order expression

$$\nu_{\pm 1/2} = |-\nu_I \pm \frac{1}{2}(a_{iso} + T_\perp(3\cos^2\theta - 1))| \quad (6)$$

where θ is the angle between the Mn−H direction and the magnetic field. The relation between θ and the angles relevant in the single-crystal experiment is described in eq 4, and because of the axial symmetry of the hyperfine interaction, ϕ and α are taken as zero.

The values of a_{iso}, $T_\perp$, β, and γ for each proton were obtained from best-fit simulations of the ENDOR rotation patterns of the $M_S = \pm 1/2$ manifolds. The crystallographic coordinates of the protons (x,y,z) were

(35) Gromov, I.; Krymov, V.; Manikandan, P.; Arieli, D.; Goldfarb, D. *J. Magn. Reson.* **1999**, *139*, 8−17.
(36) Meirovitch, E.; Luz, Z.; Kalb, A. J. *J. Am. Chem. Soc.* **1974**, *96*, 7538−7541.
(37) The program was written by Ricardo Blank and is described in: Carmieli, R. Study of Metal Binding Sites in Metalloproteins and Peptide−Membrane Interactions by Advanced EPR Spectrscopy. Ph.D. Thesis, Weizmann Institute of Science, Israel, 2005.

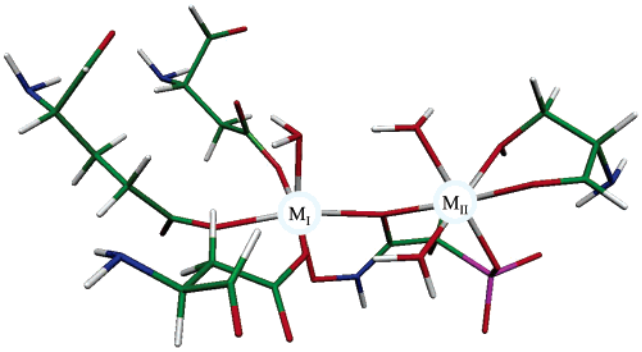

Figure 3. Model of the enolase active site chosen for the theoretical study. Sites M_I and M_{II} are either occupied as $M_I = Mn^{2+}$ and $M_{II} = Zn^{2+}$ or as $M_I = Zn^{2+}$ and $M_{II} = Mn^{2+}$.

obtained from r, β, and γ, and the coordinates of the Mn^{2+} were from the crystal structure.

3. DFT Calculations. The geometry optimization was performed on the enolase active site models using the Gaussian 2003 package[38] with the BP86 functional,[39] using the LanL2DZ basis set.[40,41] It consists of the Los Alamos effective core potentials[40] with an associated double-valence basis for metals and the Dunning Huzinaga[41] all-electron polarized double-ζ basis for main group atoms. The model structure chosen for the theoretical studies consisted of 81 atoms and was based on molecule B of the X-ray structure (Figure 3). In constructing the model, hydrogen atoms have been added to all carbon atoms in order to form appropriately hybridized atoms in the chain. Since the experimental evidence is in favor of mixed occupation of the two metal binding sites M_I and M_{II} by Mn^{2+} and Zn^{2+}, both possibilities have been considered for all of the structures used. A total of six structures were generated; (a) structures **1**(Mn/Zn) and **2**(Zn/Mn) are based on the X-ray coordinates with only the positions of the added hydrogen atoms optimized; (b) structures **3**(Mn/Zn) and **4**(Zn/Mn) were obtained from the X-ray structure following unconstrained geometry optimizations as described earlier in this paper; and (c) structures **5**(Mn/Zn) and **6**(Zn/Mn) were obtained from constrained geometry optimizations. The latter set of structures appeared to be necessary since the optimized structures showed some undesirable features. Specifically, the following constraints were applied for models **5** and **6**: (a) the distance of the $Mn-OH_2$ (O_{1014} in site II) was kept frozen at 2.186 Å; and (b) the dihedral angle between the carboxylic groups of Asp746 and Glu795, the metal in site I, and the bridging oxygen was kept frozen.

The ZFS parameter calculations were done with the ORCA program,[42] using the BP86 functional together with the CP(PPP) basis set[43] for the metal, the TZVP[44] basis set for the atoms in the first coordination sphere, and the SV(P)[45] basis on the remaining atoms. The theory of the ZFS within DFT has been discussed in a number of recent papers and will not be fully reviewed here. The prediction of the ZFS involves two complicated interactions, the direct electron−electron spin−spin (SS) coupling, which enters to first order in perturbation theory and the spin−orbit coupling (SOC), which gives contributions to the **D** tensor to second order in perturbation theory. Within spin-unrestricted DFT, the SS part is calculated as[14,46,47]

$$\mathbf{D}_{kl}^{(SS)} = \frac{g_e^2}{4}\frac{\alpha^2}{S(2S-1)}\sum_{\mu\nu}\sum_{\kappa\tau}\{\mathbf{P}_{\mu\nu}^{\alpha-\beta}\mathbf{P}_{\kappa\tau}^{\alpha-\beta} - \mathbf{P}_{\mu\kappa}^{\alpha-\beta}\mathbf{P}_{\nu\tau}^{\alpha-\beta}\}\langle\mu\nu|r_{12}^{-5}\{3r_{12,k}r_{12,l} - \delta_{kl}r_{12}^2\}|\kappa\tau\rangle \quad (7)$$

with no approximations made to the integrals. Here, S is the total spin of the electronic ground state (=5/2 for Mn^{2+}), g_e (=2.002319...) is the free-electron g value, α (~1/137) is the fine structure constant, and $\mathbf{P}^{\alpha-\beta}$ is the spin-density matrix in the atomic orbital basis $\{\varphi_\mu\}$, which is used to expand the molecular spin orbitals as $\Psi_p^\sigma = \sum_\mu c_{\mu p}^\sigma \varphi_\mu$ with orbital energies ϵ_p^σ (p = i and a refers to occupied and unoccupied spin orbitals, respectively). The operator $r_{12}^{-5}\{3r_{12,k}r_{12,l} - \delta_{kl}r_{12}^2\}$ represents the dipolar spin−spin coupling between a pair of electrons. While it was previously found that the SS interaction is more accurately predicted by open-shell spin-restricted DFT methods for organic triplets and biradicals through a complicated error compensation, this is not true to the same extent for Mn^{2+}, and our conclusions remain unchanged, independent of whether the SS part is calculated with spin-restricted or unrestricted DFT calculations. A detailed evaluation study of all parts of the ZFS for Mn^{2+} is outside of the scope of this article and will be published separately.

The SOC contribution to the **D** tensor in this work has been calculated by the method of Pederson and Khanna (PK),[48] which leads to the following form

$$\begin{aligned}\mathbf{D}_{KL}^{(SOC)} = &-\frac{1}{4S^2}\sum_{i_\beta,a_\beta}\frac{\langle\psi_i^\beta|h_K^{SOC}|\psi_a^\beta\rangle\langle\psi_a^\beta|h_L^{SOC}|\psi_i^\beta\rangle}{\epsilon_a^\beta - \epsilon_i^\beta}\\ &-\frac{1}{4S^2}\sum_{i_\alpha,a_\alpha}\frac{\langle\psi_i^\alpha|h_K^{SOC}|\psi_a^\alpha\rangle\langle\psi_a^\alpha|h_L^{SOC}|\psi_i^\alpha\rangle}{\epsilon_a^\alpha - \epsilon_i^\alpha}\\ &+\frac{1}{4S^2}\sum_{i_\alpha,a_\beta}\frac{\langle\psi_i^\alpha|h_K^{SOC}|\psi_a^\beta\rangle\langle\psi_a^\beta|h_L^{SOC}|\psi_i^\alpha\rangle}{\epsilon_a^\beta - \epsilon_i^\alpha}\\ &+\frac{1}{4S^2}\sum_{i_\beta,a_\alpha}\frac{\langle\psi_i^\beta|h_K^{SOC}|\psi_a^\alpha\rangle\langle\psi_a^\alpha|h_L^{SOC}|\psi_i^\beta\rangle}{\epsilon_a^\alpha - \epsilon_i^\beta}\end{aligned} \quad (8)$$

Here, h_K^{SOC} represents the K'th spatial component of a reduced SOC[7] operator ($K,L = x,y,z$), and ψ_p^σ are the Kohn−Sham orbitals of spin $\sigma = \alpha, \beta$ and orbital energy (p = i and a have the same meaning as the above unoccupied spin-orbitals). The relative merits of this approximation were recently discussed.[9,10] Quite typically, the PK and related DFT methods underestimate the SOC contribution to the ZFS in transition-metal complexes by up to a factor of 2, which has been attributed to the incorrect treatment of the spin-flip terms.[9,11−13,49] A similar behavior has recently also been found for diatomic molecules.[10,49] As will be discussed in detail elsewhere, the same conclusion cannot be simply carried over to the case of Mn^{2+} where the physical origin of the small, observed D values is particularly complex. The SOC operator in eq 8 was, in the present work, represented by the

(38) Frisch, M. J.; et al. *Gaussian 03*, revision B.04; Gaussian, Inc.: Wallingford, CT, 2004.
(39) (a) Becke, A. D. *Phys. Rev. A* **1988**, *38*, 3098−3100. (b) Perdew, J. P. *Phys. Rev. B* **1986**, *33*, 8822−8824. (c) Perdew, J. P. *Phys. Rev. B* **1986**, *34*, 7406−7406.
(40) (a) Hay, P. J.; Wadt, W. R. *J. Chem. Phys.* **1985**, *82*, 270−283. (b) Wadt, W. R.; Hay, P. J. *J. Chem. Phys.* **1985**, *82*, 284−298. (c) Hay, P. J.; Wadt, W. R. *J. Chem. Phys.* **1985**, *82*, 299−310.
(41) Dunning, T. H.; Hay, P. J., Jr. In *Modern Theoretical Chemistry*; Schaefer, H. F., Ed.; Plenum: New York, 1976; Vol. III, pp 1−28.
(42) Neese, F. *ORCA*, version 2.5.00; Universität Bonn: Bonn, Germany. The program is available free of charge at http://www.thch.uni-bonn.de/tc/orca.
(43) Neese, F. *Inorg. Chim. Acta* **2002**, *337*, 181−192. The CP(PPP) basis is a minor modification of the double-ζ basis set developed by Ahlrichs and co-workers, which was obtained from the TurboMole library at ftp.chemie.uni-karlsruhe.de/pub/basen' (2002).
(44) Schäfer, A.; Huber, C.; Ahlrichs, R. *J. Chem. Phys.* **1994**, *100*, 5829−5835.
(45) Schäfer, A.; Horn, H.; Ahlrichs, R. *J. Chem. Phys.* **1992**, *97*, 2571−2577.
(46) Petrenko, T. T.; Petrenko, T. L.; Bratus, V. Y. *J. Phys.: Condens. Matter* **2002**, *14*, 12433−12440.
(47) Shoji, M.; Koizumi, K.; Hamamoto, T.; Taniguchi, T.; Takeda, R.; Kitagawa, Y.; Kawakami, T.; Okumura, M.; Yamanaka, S.; Yamaguchi, K. *Polyhedron* **2004**, *24*, 2708−2715.
(48) Pederson, M. R.; Khanna, S. N. *Phys. Rev. B* **1999**, *60*, 9566−9572.
(49) Reviakine, R.; Arbuznikov, A.; Tremblay, J.-C.; Remenyi, C.; Malkina, O. L.; Malkin, V. G.; Kaupp, M. *J. Chem. Phys.* **2006**, *125*, 054110-1−054110-12.

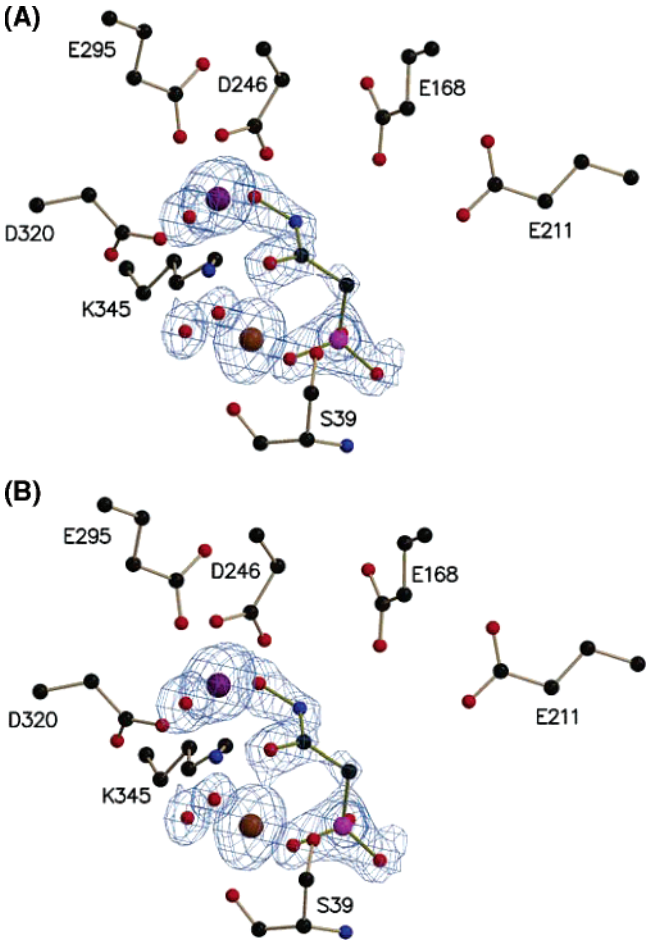

Figure 4. Stereoview of key active site residues of subunit 2. Color code: pink, phosphorus; red, oxygen; blue, nitrogen; gray, carbon; purple, Zn^{2+}; brown, Mn^{2+}. The F_o-F_c electron density map, contoured at 5σ, is shown for PhAH, the metal ions, and the three water molecules that are ligands to the metal ions. The Zn^{2+} and the Mn^{2+} ions are arbitrarily placed in sites I and II, respectively.

spin−orbit mean-field (SOMF) approximation,[50] the implementation of which is described in ref 51, and with density fitting for the Coulomb contribution of the SOMF operator.

Results

Crystal Structure. The crystal properties of the enolase (Zn^{2+}/Mn^{2+})−PhAH complex are summarized in Table 1. It forms a dimer, and the conformations of the subunits of the enolase (Zn^{2+}/Mn^{2+})−PhAH complex are almost identical. The three loops regions, residues 37−43 (loop 1), 153−166 (loop 2), and 251−275 (loop 3), have the same conformation for both subunits. The rms deviation between the two subunits is 0.26 Å, with a maximum deviation of 1.8 Å for Asn80. Loop 1 is in the closed conformation. Loop 2 is in the open conformation, with disordered residues 158−162 in subunit 1 and 159−161 in subunit 2. Loop 3 is in an open conformation.

Figure 4 shows the F_o-F_c density map, contoured at 5σ, for the inhibitor, the metal ions, and the surrounding water molecules; each is clearly defined by the density. The figure

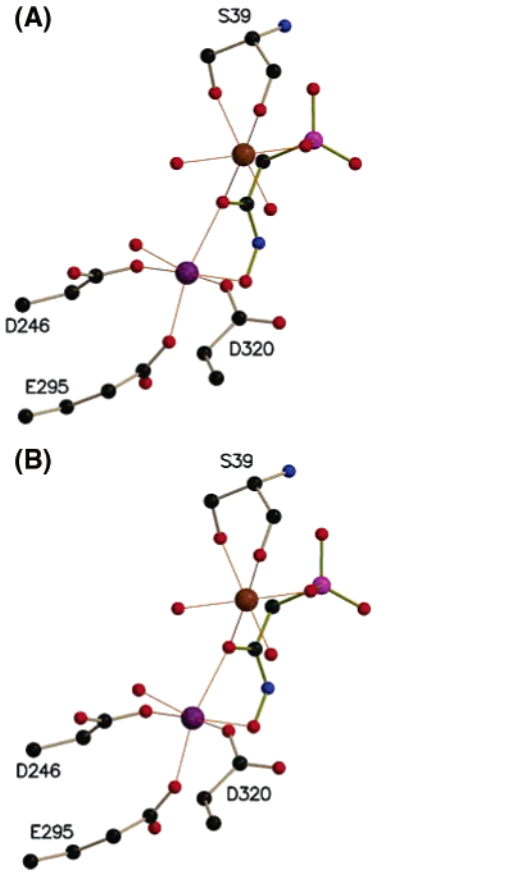

Figure 5. Stereoview of the coordination of the two metal ions in the enolase (Zn^{2+}/Mn^{2+})−PhAH complex. The orange lines show the coordination for the metal ions.

arbitrarily shows Zn^{2+} in site I and Mn^{2+} in site II. Figure 5 is a stereoview of the active site depicting the complete coordination of both metal sites.

An overlay of the active sites of the Mg^{2+}−PhAH complex[22] versus the (Zn^{2+}/Mn^{2+})−PhAH complex (Figure 6) shows that the catalytic residues Lys345, Glu168, and Glu211 are virtually unchanged. The position of Ser39 is also essentially unchanged. Loop 2, which includes His159, in the Mg^{2+}−PhAH structure is in the closed conformation. In the (Zn^{2+}/Mn^{2+})−PhAH structure, loop 2 is in the open conformation with His159 disordered. The positions of the metal ions are slightly different between the two complexes. The overlay shows a difference in position of <0.4 Å for site I and <0.6 Å for site II.

EPR Experiments. Single crystals of enolase (Zn^{2+}/Mn^{2+})−PhAH with a well-defined morphology were mounted into thin-walled quartz tubes in two orientations. On the basis of the morphology of the crystal, a reference a' axis was defined, as shown in Figure 2. Measurements were carried out on two crystals, one mounted with a' parallel to the tube axis and one with a' perpendicular to it. CW−EPR spectra were recorded as a function of orientation at room temperature and at 4.5 K to check whether the Mn^{2+} sites exhibit any dynamics similar to that found in crystals of concanavalin A.[4] In contrast to concanavalin A, despite the considerable differences in S/N, the room- and low-temperature spectra were found to be similar (not shown).

FS−ED EPR spectra, recorded as a function of the rotation angle in the two planes described above, are shown in Figure 7a and b. On the basis of the preparation method, Mn^{2+} was

(50) Hess, B. A.; Marian, C. M.; Wahlgren, U.; Gropen, O. *Chem. Phys. Lett.* **1996**, *251*, 365−371.
(51) The implementation is described in Neese, F.; Wolf, A.; Fleig, T.; Reiher, M.; Hess, B. A. *J. Chem. Phys.* **2005**, *122*, 204107-1−204107-10, while the identical equation has previously been derived in Berning, A.; Schweizer, M.; Werner, H. J.; Knowles, P. J.; Palmieri, P. *Mol. Phys.* **2000**, *98*, 1823−1833.

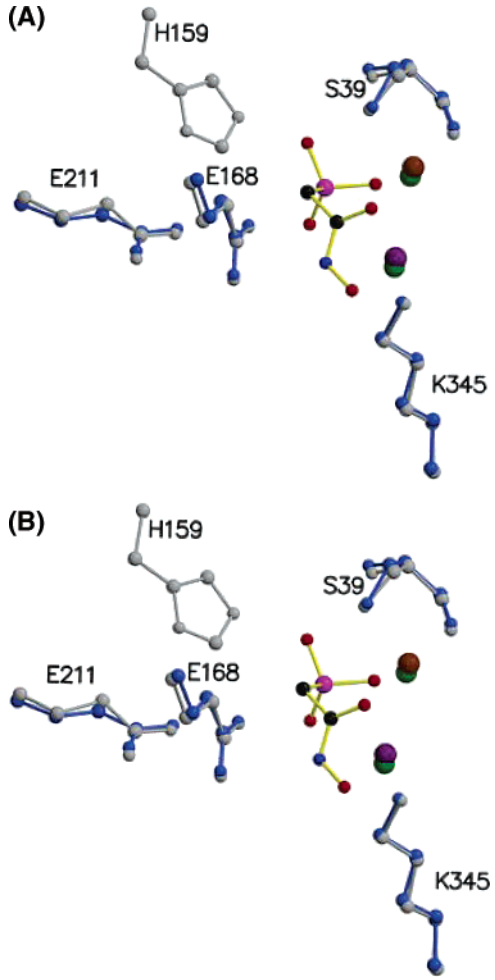

Figure 6. Overlay of the active sites of the enolase (Zn^{2+}/Mn^{2+})−PhAH complex and the enolase Mg^{2+}−PhAH complex.[22] The residues of the enolase (Zn^{2+}/Mn^{2+})−PhAH complex are shown in blue. The green spheres represent the Mg^{2+} ions. The residues of the enolase Mg^{2+}−PhAH complex are shown in silver. In the overlay, the position of PhAH for the Mg^{2+} complex is virtually identical to that in the Zn^{2+}/Mn^{2+} complex, and therefore, only the PhAH from the Zn^{2+}/Mn^{2+} complex is shown.

initially believed to primarily occupy site II, while Zn^{2+} was mostly in site I.[19] Hence, signals of four magnetically inequivalent Mn^{2+} ions situated at site II were expected for an arbitrary orientation because there are two dimers per unit cell. The FS−ED EPR rotation patterns and their best-fit simulations are shown in Figure 8. These reveal five resolved peaks in the region around 140° of the $a' \perp B$ plane, showing that there are more than four symmetry-related Mn^{2+} sites. This is attributed to site exchange between the Zn^{2+} at site I and Mn^{2+} at site II, which has taken place during or after the crystal growth. A similar exchange has been observed in solution between Mn^{2+} in site II and Mg^{2+} in site I.[20] In the fitting procedure, the ^{55}Mn hyperfine coupling, *A*, and the ZFS tensors (**D**) were initially obtained by a best-fit procedure of both planes simultaneously, without applying any symmetry constraints. It was carried out for both the highest and lowest field ^{55}Mn hyperfine components to ensure that the correct spectroscopic characteristics of each site were considered. Then, based on the crystal symmetry, the individual rotation patterns which gave close *A*, *D*, and *E* values were forced to have the same values. The best-fit procedure was then applied again for all four sites with the same *D* and *E* values, allowing only for individual fitting of α, β, and γ for

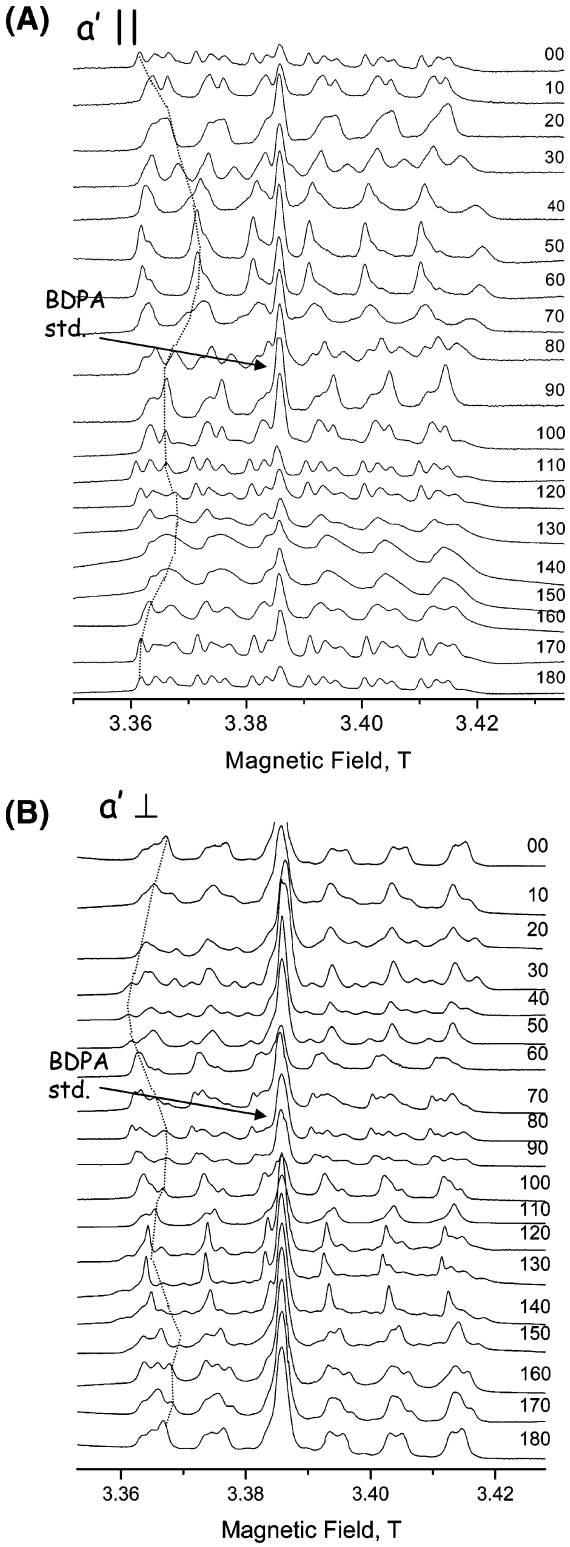

Figure 7. The orientation dependence of the FS−ED W-band EPR spectra of a single crystal of enolase (Mn^{2+}/Zn^{2+})−PhAH; (A) *a′* parallel to the tube axis defined as 0°, 0°, 0° for the morphology to tube transformation; (B) *a′* perpendicular to the tube axis defined as 0°, 90°, 0° for the morphology to tube transformation. The rotation angles (in degrees) are noted on the figure. The dotted lines mark the signals of Mn_{A2}.

each site. This gave the orientation of the ZFS tensor with respect to the morphology frame. Next, the relation between the crystal and the morphology frames was determined (see Supporting Information). This finally provided the orientation

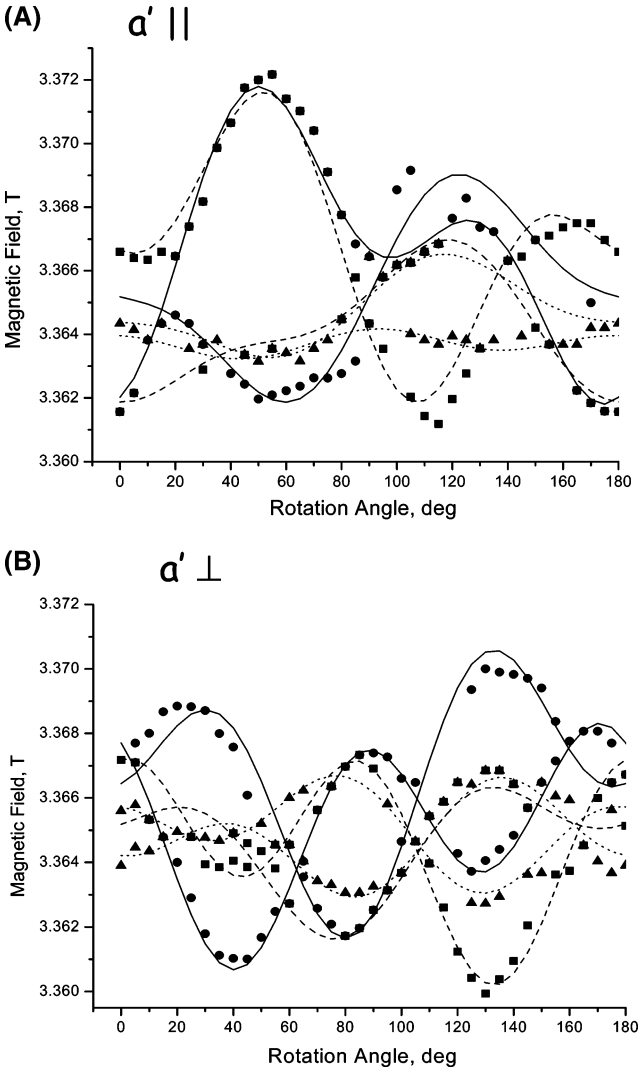

Figure 8. Rotation patterns of the lowest-field ^{55}Mn hyperfine component of a single crystal enolase (Mn^{2+}/Zn^{2+})−PhAH measured at 4.5 K; (A) a' axis parallel to the tube axis; (B) a' axis perpendicular to the tube axis. The lines are the best-fit simulation traces; Mn_{A1} and Mn_{A2} solid lines (circles), Mn_{A3} and Mn_{A4} dashed lines (squares), and Mn_{B1} and Mn_{B2} dotted lines (triangles).

of **D** with respect to the cartesian crystal frame, as listed in Table 2. The analysis was not sensitive enough to the sign of D, and therefore, a positive value was chosen arbitrarily. This is actually expected because in most of the terms in eq 2 D^2 appears.

The EPR rotation pattern analysis gave four sites of Mn_A^{2+} with $D = 73$ mT and $(E/D) = 0.16$ and two sites of Mn_B^{2+} with $D = 45.9$ mT and $(E/D) = 0.19$. For both sites, $A = 9.5$ mT. The two other Mn_B^{2+} sites could not be determined due to resolution limitation of the EPR spectra. Two pairs within each type are related by a 180° rotation according to the crystal symmetry. The pairs found were Mn_{A1} and Mn_{A2} noted by solid lines, Mn_{A3} and Mn_{A4}, represented by dashed lines in Figure 8. In this figure, Mn_{B1} and Mn_{B2} are represented by dotted lines. The results are summarized in Table 2 where α, β, and γ are the angles of the ZFS reference frame relative to the morphology reference frame; α', β', and γ' are the angles relating the crystal and morphology reference frames, as determined from each pair. Obviously, these should all yield the same set of angles, and indeed, the values obtained from the symmetry-related Mn_A pairs are close. Finally α, β, and γ are the angles relating the ZFS reference frame with the crystal Cartesian reference frame, as defined in the protein data bank (PDB). The large discrepancy between α',β',γ' of Mn_B and those of Mn_A is probably because only two Mn_B were found, and this pair is not related by the crystal symmetry but within the dimer; hence, we used the set obtained from the Mn_A results.

Next, we proceeded to place the ZFS principal axis systems on the structure of the Mn^{2+} binding sites. Because there are two dimers in the unit cell and because each monomer contains two Mn^{2+} ions, there are eight possibilities to orient each of the experimental **D**'s with respect to the metal binding sites in the crystal structure. Tables 3 and 4 summarize all of these possibilities, where only one dimer was considered, and only orientations for which any of the x, y, or z principal axes make an angle smaller than 27° with any of the six Mn−O directions are listed. Although none of the options showed alignment along the Mn−O directions, some were close enough, Mn_{A3} with respect to site I in molecule A and Mn_{A2} with respect to site I in molecule B. Here, the z axis points approximately along the M−O direction of the bridging oxygen in PhAH, as shown in Figure 9. These orientations of **D** of Mn_{A2} and Mn_{A3} show that a 180° rotation about the z axis relates the ZFS of the Mn^{2+} of site I in molecules A and B in the same dimer. Using similar arguments, all four Mn_A sites were assigned to all four enolase subunits in the unit cell, as listed in Table 2. The possible orientations of **D** of Mn_A with respect to site II show that, for Mn_{A2} and Mn_{A3}, the x, y, and z axes are also approximately along the Mn−O directions, but the two differ in terms of the orientation of the specific axes and, therefore, cannot be associated with the same type of site. Hence, the assignment of Mn_A to site I is more plausible. This is further supported by its large D value, which suggests a larger deviation from octahedral symmetry. While the differences in Mn−O distances seem similar for the two sites, the angles between the Mn−O directions deviate from 90/180° of a perfect octahedral symmetry more in site I.

As opposed to Mn_A, none of the possible orientations of **D** of Mn_B show an approximate alignment of all x, y, and z along the Mn−O direction in site II of molecule A or B. This is expected because this site does not show any critical constraints. Figure 9 shows one of the options, Mn_{B1}, with respect to site II in molecule B. To further support the assignment of Mn_A to site I, ENDOR measurements were carried out.

ENDOR Measurements. The coordination shells of Mn^{2+} in sites I and II differ in the number of water ligands; site II has two water ligands, whereas site I has only one. Moreover, site II exhibits a Mn−O−P coordination, and therefore, ^{31}P ENDOR signals are expected. Hence, the ENDOR results can be used to assign Mn_A and Mn_B to their respective sites. Complete rotation patterns of ^1H ENDOR spectra were recorded by setting the magnetic field at each of the resolved low-field ^{55}Mn hyperfine components of the central EPR transition. However, only after the EPR rotation patterns were fully analyzed was it possible to proceed and assign the ENDOR signals to a particular site through the individual EPR rotation patterns found. This allowed construction (isolation) of the individual ^1H ENDOR rotation patterns of the specific Mn^{2+} sites. Figure 10 shows the orientation-dependent ENDOR spectra recorded with the magnetic field set to the EPR signal of Mn_{A2}.

Table 2. Summary of the ZFS Parameters Obtained from the Best Fit of the FS−ED EPR Rotation Patterns and Those Calculated Using DFT and SPM

type	D, mT (±1)[d]	E/D (±0.02)	α,β,γ (±5°)	α′,β′,γ′ (±5°)	α″,β″,γ″ (±5°)	assignment
Mn_{A1}	±73.0	0.16	155, 39, 30	350, 40, 320	168, 77, 333	mol B, dimer II
Mn_{A2}	±73.0	0.16	33, 118, 275	350, 40, 320	−9, 108, 208	mol B, dimer I
Mn_{A3}	±73.0	0.16	27, 59, 163	340, 35, 320	66, 28, 83	mol A, dimer I
Mn_{A4}	±73.0	0.16	158, 149, 89	340, 35, 320	224, 136, 93	mol A, dimer II
Mn_{B1}	±45.9	0.19	4, 156, 227	260, 30, 160	−22, 119, 156	
Mn_{B2}	±45.9	0.19	150, 43, 216	260, 30, 160	80, 17, −130	
Mn(**1**)[a]	−206.5(−137.7)[e]	0.27				site I, DFT
Mn(**3**)	51(34)	0.28				site I, DFT
Mn(**5**)	−313.5(−209)	0.31				site I, DFT
Mn(**2**)	−370.5(−247)	0.28				site II, DFT
Mn(**4**)	−147.3(−98.2)	0.15				site II, DFT
Mn(**6**)	−237.6(−158.4)	0.14				site II, DFT
Mn[b]	−41.0	0.26			36.2, 87.2, 4.0	site I, SPM (mol B)
Mn[c]	17.0	0.02			246, 83, 201	site I, SPM (mol A)
Mn[c]	−24.3	0.20			270, 43, 73	site II, SPM (mol A)
Mn[b]	−38.0	0.23			210, 35, 93	site II, SPM (mol B)

[a] The number in parentheses corresponds to the DFT structure mentioned in the text. [b] Calculated using the coordinates of molecule B in the crystal structure. [c] Calculated using the coordinates of molecule A in the crystal structure. [d] The error corresponds only to the experimental results. [e] The values in parentheses were scaled by 2/3 (for explanation, see DFT section).

Table 3. Possible Orientations of the Principal Axes of the ZFS of Mn_A and Mn_B Relative to Specific Mn−Ligand Directions (in Degrees) for Molecule A[a]

		Site I		Site II	
		angles	Mn–O	angles	Mn–O
Mn_{A1}	z	16/166	O(PhAH)/O(W)		
Mn_{A2}	x			23/164	O(W)/O(Ser39)
	y			27/154	O(PhAH)/O(Ser39)
	z			156/22	OP(PhAH)/O(W)
Mn_{A3}	x	18/167	O(PhAH)/O(W)		
	y	153/17	O(Asp246)/O(Asp320)		
	z	25/159	O(PhAH)/O(Glu295)		
Mn_{A4}	x	156/27	O(PhAH)/O(Glu295)		
Mn_{B1}	x			156/27	O(W)/O(Ser39)
	y	153/23	O(PhAH)/O(Glu295)	27/153	O(PhAH)/O(Ser39)
Mn_{B2}	x	139/24	O(PhAH)/O(W)		
	z			167/19	O(W)/O(Ser39)

[a] Only possibilities with x, y, or z making an angle less than 27° with any Mn−ligand direction are listed.

Table 4. Same as Table 3 but for Molecule B

		Site I		Site II	
		angles	Mn–ligand	angles	Mn–O
Mn_{A1}	x	25/143	O(PhAH)/O(W)	9/177	OP(PhAH)/O(W)
	y			156/23	O(PhAH)/O(Ser539)
	z	17/153	O(Asp820)/O(Asp746)	25/149	O(W)/O(Ser539)
Mn_{A2}	x	172/6	O(PhAH)/O(W)		
	y	20/167	O(Asp820)/O(Asp746)		
	z	21/162	O(PhAH)/O(Glu795)		
Mn_{A3}	x	16/155	O(Asp820)/O(Asp746)		
Mn_{A4}	x	6/167	O(PhAH)/O(Glu795)		
Mn_{B1}	x	154/20	O(PhAH)/O(W)		
Mn_{B2}	x	171/4	O(Asp820)/O(Asp746)	156/27	OP(PhAH)/O(W)
	y	165/7	O(PhAH)/O(Glu795)		
	z	175/8	O(PhAH)/O(W)		

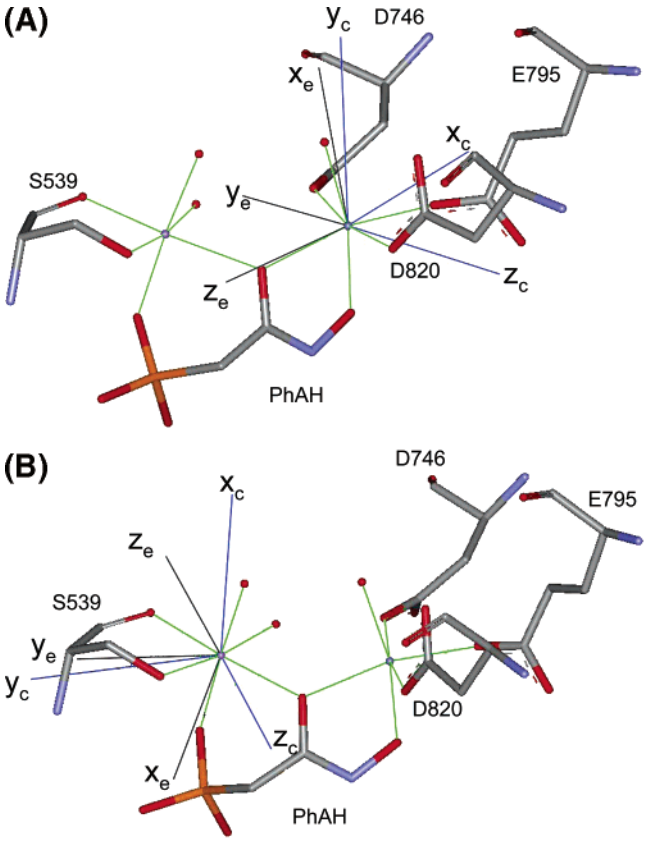

Figure 9. The orientation of the principal axes (x_e,y_e,z_e) of the experimental ZFS tensors (black lines) of (A) Mn_{A2} with respect to site I in molecule B, dimer I and (B) Mn_{B1} with respect to site II, molecule B (same dimer) along with the principal axes (x_c,y_c,z_c) of the DFT-calculated tensors of structures **1** and **2**, respectively.

Its EPR signals are also indicated in Figure 7. This site was chosen because its rotation pattern was more resolved (see Figure 8), although there are still orientations where it overlaps with other sites. The rotation patterns of these ENDOR signals are presented in Figure 11. The rotation patterns are complicated and include contributions from many protons, not all from Mn_{A2}. We focused on those with large couplings, which are likely to be due to water ligands because all other protons in the protein and PhAH (the OH is expected to be deprotonated) are at $r >$ 3.65 Å. The analysis was similar to that of the EPR rotation patterns; the best fit gave the hyperfine tensor with respect to the morphology frame-of-reference. Then, the Euler angles obtained were transformed into the orthogonal crystal frame using the Euler angles determined by the analysis and the EPR signals. Four different protons were identified. The rotation patterns of H_{w1}, H_{w2}, H_{w3}, and H_{w4} in the two planes are presented in Figure 11, and the a_{iso}, $T_\perp$, β and γ, and r values

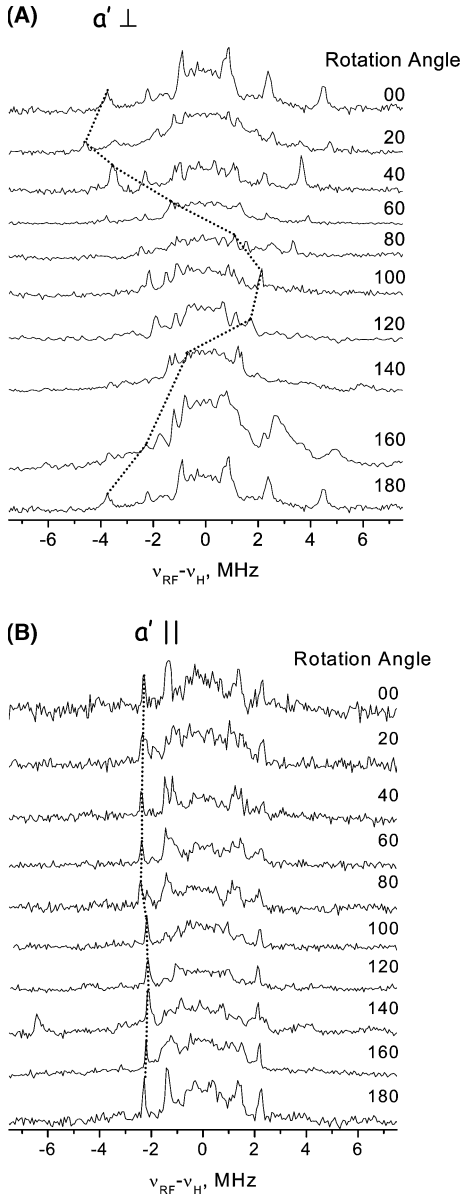

Figure 10. Orientation-dependent ^{1}H ENDOR spectra collected along the EPR rotation pattern of Mn_{A2} in two planes; (A) *a*′ axis perpendicular to the tube axis; (B) *a*′ axis parallel to the tube axis. The ENDOR frequencies were corrected for a uniform nuclear Larmor frequency to remove the field dependence of the EPR lines. The dotted line represents the signals of H_{w2}.

obtained are listed in Table 5. H_{w1} and H_{w2} belong to a water ligand of Mn^{2+} in site I, while the other two are more distant. Attempts to analyze the ENDOR results with two water ligands, namely, four protons at a distance of 2.6−2.8 Å, as expected for site II, did not result in a satisfactory fit.

The assignment of the protons was done as follows. Their coordinates were calculated using the Mn−H distance and orientation obtained from the ENDOR results and the Mn coordinates from the crystal structure. Then, the protons were added to the crystal structure relative to the Mn in sites I and II, and using the water−oxygen coordinates, the O−H and H−H distances were calculated to verify that the positions were reasonable. This resulted in the assignment of four protons to two water molecules with O_{1015}−H_{w1} and O_{1015}−H_{w2} distances of 0.99 and 0.95 Å, respectively, and a $HO_{1013}H$ angle of 101.3°. The distance between H_{w1} and H_{w2} is 1.5 Å. In the second water molecule, the H_{w3}−H_{w4} distance is 1.55 Å, the O_{1013}−H_{w3} and O_{1013}−H_{w4} distances are 0.98 and 0.96 Å, respectively, and the $HO_{1015}H$ angle is 106°. The O_{1015} water molecule is a ligand of the Mn^{2+} in site I, while O_{1013} is a ligand to Zn^{2+} in site II, but its protons are relatively close also to the Mn^{2+} in site I. These results are consistent with the assignment of Mn_A to site I, which has only one water ligand. The protons' coordinates also show that the two water molecules are involved in hydrogen bonds with Asp820, Glu795, Asp746, PhAH, and O_{1014}, forming a hydrogen-bond network, stabilizing the tertiary structure of the protein with the inhibitor (Figure 12).

We tried to measure ^{31}P and ^{14}N ENDOR but failed to detect any ENDOR signals. While ^{14}N ENDOR signals of weakly coupled nuclei are difficult to observe at the W-band, ^{31}P in a Mn−O−P environment is known to exhibit a_{iso} values around 4−6 MHz.[52−54] The absence of ^{31}P ENDOR signals, expected for Mn^{2+} in site II, may be attributed sensitivity limitations. The ^{31}P signals can also be broad in a single crystals[50] and, therefore, may have escaped detection.

Theoretical Models

DFT Calculations. The EPR and ENDOR measurements described previously in this paper yielded two types of Mn^{2+}, differing in their ZFS tensors. Their assignment to the specific sites I and II was based on the ^{1}H ENDOR results, which identified one water ligand, as expected for site I, and revealed the interaction with protons 3.2 Å away, belonging to a water ligand on the Zn^{2+} in site II. Moreover, the larger deviation of site I from octahedral symmetry suggests that its *D* value should be larger. In addition, the directions of the *x*, *y*, and *z* axes of the ZFS of Mn_A were found to point relatively close to the M−O directions. However, considering the complexity of the system and the congested ENDOR spectra, all of these considerations make the assignment to site I more probable but not unambiguous. Encouraged by the results of recent applications of DFT methods to calculate zero-field splittings, showing that experimental trends are usually well reproduced for series of related compounds,[9−14] we have applied these methods to the Mn^{2+} binding sites in the enolase−PhAH system to verify the assignment of the experimentally determined tensors to their respective sites. In addition, it will allow for further evaluation of the performance of the DFT methods to protein sites with relatively small ZFS.

As explained in detail in the Experimental Section, three model clusters for the Mn−PhAH−Zn enolase active site were considered. These models contain Mn^{2+} in either site I or site II and a Zn^{2+} ion in the other site, thus leading to a total of six structures that were investigated theoretically. Structures **1**(Mn/Zn) and **2**(Zn/Mn) are based on the X-ray structure and contain Mn^{2+} in sites I and II, respectively, with only the positions of the added hydrogen atoms optimized. Structures **3**(Mn/Zn) and **4**(Zn/Mn) were fully optimized. However, several problems became apparent in the optimizations. The main shortcomings were a very long (2.48 Å) Mn−OH_2 bond, which appears to be unreasonable, and a significant tilt of the carboxylate/Mn/

(52) Arieli, D.; Delabie, A.; Groothaert, M.; Pierloot, K.; Goldfarb. D. *J. Phys. Chem. B* **2002**, *106*, 9086−9097.
(53) Walsby, C. J.; Telser, J.; Rigsby, R. E.; Armstrong, R. N.; Hoffman, B. M. *J. Am. Chem. Soc.* **2005**, *127*, 8310−8319.
(54) Arieli, D.; Prisner, T. F.; Hertel, M.; Goldfarb, D. *Phys. Chem. Chem. Phys.* **2004**, *6*, 172−181.

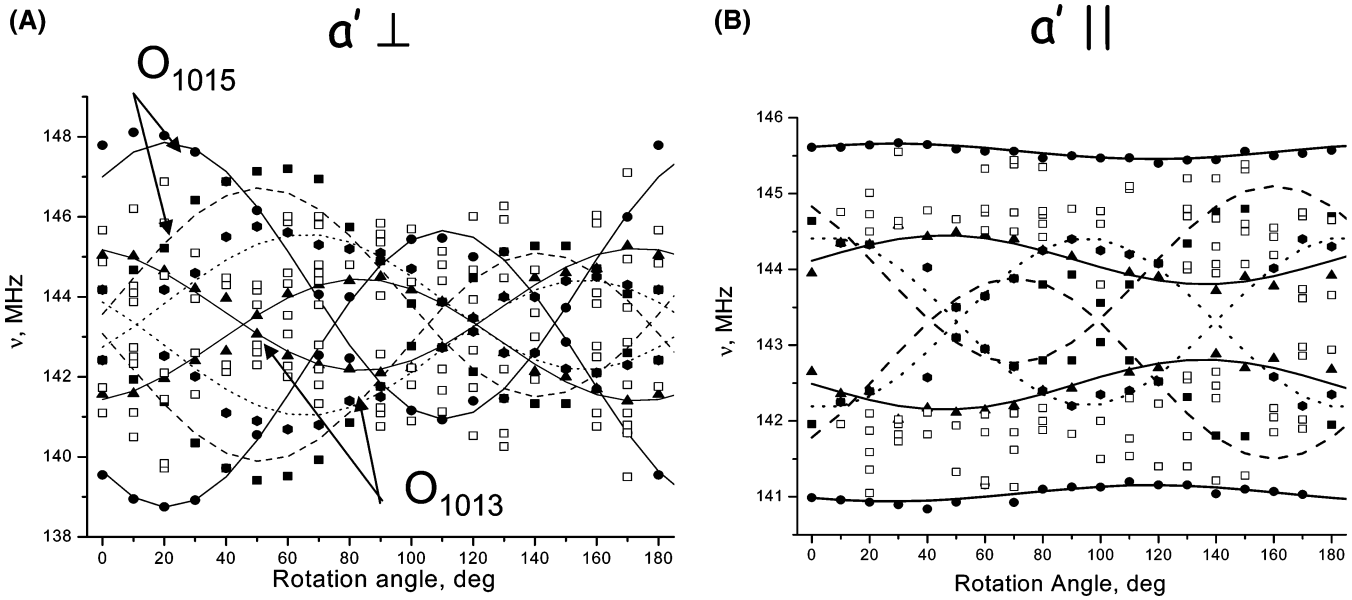

Figure 11. ^{1}H ENDOR rotation pattern of the spectra shown in Figure 10 and best-fit simulations in the two planes; (A) a' axis perpendicular to the tube axis; (B) a' axis parallel to the tube axis. H_{w1}: dashed line. H_{w2}: solid line. H_{w3}: dotted line. H_{w4}: gray line. The filled symbols represent signals belonging to these protons.

Table 5. Summary of Best-Fit Hyperfine Parameters of the Protons of Two Water Molecules[a]

proton	$T_\perp$ (± 0.04) MHz	a_{iso} (± 0.04) MHz	β ± 0.5°	γ ± 0.5°	r_{Mn-H} Å ± 0.02
H_{w1}	3.78	0.18	60.3(41)	−88.3(290)	2.75
H_{w2}	4.49	−0.23	34.5(10)	−54(242)	2.6
H_{w3}	2.25	0.07	54.5(54)	−114(265)	3.24
H_{w4}	2.30	−0.1	117.4(154)	155.7(224)	3.3

[a] The angles listed in parentheses are the angles calculated with respect to the morphology reference frame.

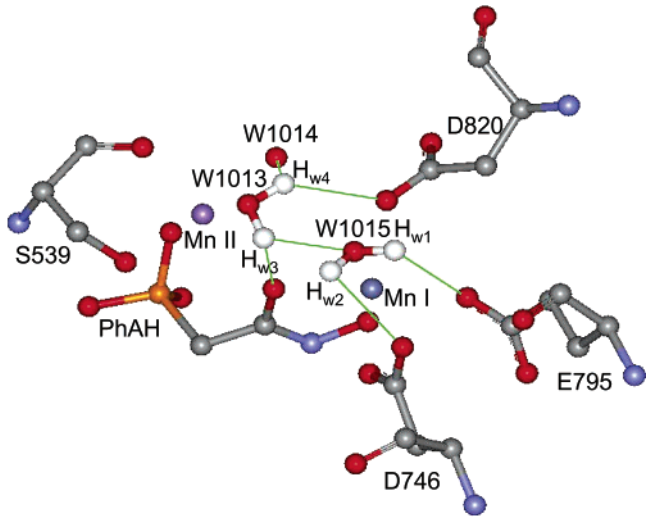

Figure 12. The structure of the active site determined by X-ray crystallography (molecule B) along with water protons, as found by the ENDOR analysis.

bridging oxygen dihedral angle, which cannot occur in the protein pocket due to the constraints imposed by the protein. Consequently, structures **5**(Mn/Zn) and **6**(Zn/Mn) were constructed in which the optimizations were carried out under the constraints of a 2.186 Å Mn−OH_2 distance and dihedral tilt angles that were frozen to the values obtained from the X-ray analysis. A comparison of the optimized structures with the

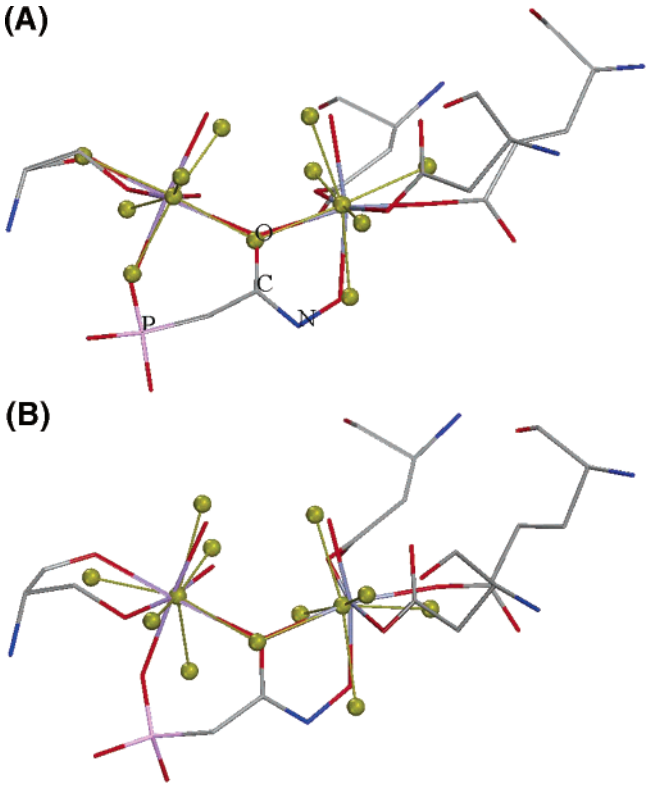

Figure 13. (A) M-matched first-coordination-sphere atoms of the totally relaxed structure **3**(Mn/Zn) with the X-ray structure **1**(Mn/Zn). (B) The same comparison of **1**(Mn/Zn) with the partially optimized structure **5**(Mn/Zn). Structure **1** is represented by sticks.

X-ray structure is provided in Figure 13. The partially optimized structure deviates from the X-ray result mainly in the position of the PO_3 fragment as well as the Asp820 residue (Figure 13, bottom). The deviation from octahedral symmetry is larger in the optimized structures than it is in the X-ray structures. Nevertheless, the two relaxed sets of coordinates show that no major change occurs in the structure after the exchange of the Mn^{2+} and Zn^{2+} ions. This may be related to the fact that both

the half-filled d shell in Mn^{2+} and the fully occupied d shell in Zn^{2+} do not lead to a strong geometric preference, which, in turn, is perhaps the reason for each ion being able to occupy either position in the actual protein.

The *D* and *E* values calculated for the six structures are listed in Table 2. In general, all of the values are on the order of the experimental ones. The low symmetry of the two enolase sites can be seen from the high *E*/*D* ratio and is consistent with the EPR results, which showed somewhat lower values. The higher rhombicity of site I renders the sign of the calculated *D* value meaningless since the positive or negative signs are equivalent for *E*/*D* approaching 1/3. For the Mn^{2+} occupying site II, all calculated *D* values are negative with a smaller rhombicity (except for structure **2**). Therefore, it is most probable that the *D* value of site II is negative. Interestingly, the calculated *D* value for the unoptimized structures **1**(Mn/Zn) and **2**(Zn/Mn) are more overestimated compared to the experimental findings than it is for the (partially) relaxed structures **3**−**6**. The variations of the *D* values within the structures demonstrate their sensitivity to the actual structure as well as the difficulty in obtaining a highly accurate structure from calculations on small parts of the protein when the active site is floppy, as is the case here. Nonetheless, considering the magnitude of *D*, a larger |*D*| value is consistently obtained for Mn^{2+} occupying site II. This is, however, inconsistent with the interpretation of the experimental data, as will be discussed in the following.

The orientations of the principal axes of the ZFS for Mn^{2+} in **3** and **4** (which gives the best agreement with experiment in terms of the amplitude of *D*) show that none of the magnetic axes coincides with any of the Mn−ligand directions, but for some axes, the deviations are not very large. For site I, the *z* axis makes an angle of 20° with the Mn−O(N) of PhAH. This is similar to the *x* direction of Mn_{A2} and Mn_{A3} in site I. The very high rhombicity, however, makes the *x* and *z* interchangeable. The orientation of the tensor of **5** (site I) did not show any correlation with the Mn−ligand directions, while that of **6** (site II) did, with *x*, *y*, and *z* approximately (deviations of 10−20°) along the O(Ser)−Mn−O(PhAH), OP(PhAH)−Mn−O(W), and O(Ser)−Mn−O(W) directions, respectively. While structure **1** gave the most overestimated |*D*| value, the tensor orientations are approximately along the Mn−ligands directions, with the *x* (*z*) axis showing a similar orientation as that of Mn_{A2} and Mn_{A3} with respect to site I, as shown in Figure 9A. The *x* and *z* cannot be distinguished because $E/D \sim 1/3$. In fact, the *z* (*x*) and *y* axes are, however, exchanged compared to the experimental directions. Interestingly, the *x* (*z*) direction is close to the Mn−O direction that exhibits the largest deviation from the octahedral axes. For structure **2**, *x* is approximately along the OP(PhAH)−Mn direction, as shown in Figure 9B. This orientation is rather close to that of Mn_{B1} with respect to site II in molecule B, considering that the axes have no polarity. The above shows that the deviations of the Mn−O directions from the octahedral symmetry axes are responsible for situating the principal axes away from the Mn−O directions. Because no single contribution to the **D** tensor of Mn^{2+} was found to be dominant, it appeared to be impossible to relate the calculated orientations to specific aspects of the electronic structure of the Mn^{2+} ion in either site.

A ^{31}P ENDOR signal with a hyperfine coupling, a_{iso}, of 4−6 MHz would be expected for site II if Mn^{2+} would occupy this site.[52−54] Since no ^{31}P signal could be detected experimentally, this coupling was calculated. As expected from distance arguments, the values $a_{iso} = 6.15$ MHz and $T = (-1.37, -0.88, 2.2)$ MHz for Mn^{2+} in site II for **4**(Zn/Mn) are within the expected range. Much smaller values were obtained for Mn^{2+} site I (**3**(Mn/Zn)): $a_{iso} = 0.28$ MHz and $T = (0.22, -0.18, 0.4)$ MHz, as expected. Hence, the absence of ^{31}P ENDOR signals for site II is, indeed, surprising and is attributed to sensitivity limitations.

In judging the quantum chemical results, it must be recalled what is involved for the task at hand. First of all, the theoretical method must predict an accurate structure since the calculations will react very sensitively to errors in the theoretical geometries, as indeed are observed for the differences between the structures used in the DFT calculations. This is particularly acute in the case of Mn^{2+}, which has a half-filled d shell, relatively weak binding to the ligands, and, consequently, no strong geometric preference. Given this, the *D* value (as opposed to the entire ZFS tensor) measures deviations from cubic symmetry and will, therefore, react very sensitively to even minor geometric distortions and small electronic effects in the binding of Mn^{2+} to its ligands, which features very limited covalent interactions. Next, the calculations involved important contributions from the spin−orbit coupling. The SOC is, inherently, a two-electron property, and it is only due to recent developments that the SOC operator itself can be accurately represented by a multicenter spin−orbit mean-field operator.[55] Still, even given an accurate SOC operator, it will couple the sextet ground state with excited states of sextet, quartet, and octet multiplicities. In fact, perhaps contrary to popular belief based on ligand field theory, all of these contributions are significant in Mn^{2+} compounds; thus, the theoretical method has to describe spin-conserving and spin-flip excitations either explicitly or implicitly in a consistent and balanced manner in order to obtain a realistic picture of the various contributions. These contributions may well be of opposite sign and partially cancel each other. Moreover, the direct spin−spin coupling term is a complicated two-electron operator with a steep inverse-third-power dependence of the interelectronic distance between unpaired electrons, and its accurate calculation is complicated. Thus, one is faced with four different contributions of similar magnitude and partially cancelling signs with the net result being a very small ZFS in the case of Mn^{2+}, which does not feature any strong electronic anisotropy. This is nicely confirmed by a recent determination of the ZFS tensor by a single-crystal W-band in an analogous high-spin Fe(III), which has a larger electronic asymmetry than that of Mn^{2+} doped into a Ga(III)−oxo dimer.[56] There, it has been found that the principal axes of the ZFS tensor do not correlate with any of the molecular axes or bond directions. It is, therefore, not too surprising that it turns out to be quite difficult to calculate the ZFS in Mn^{2+} to a high precision.

Nevertheless, the results of recent test calculations that we have carried out on a series of structurally well-characterized Mn(II) complexes with *D* values in the range of 0.1−1 T, which is larger than the value exhibited in enolase (to be published elsewhere), revealed that the calculations still correlate well with the experimental data, with an observed systematic overestimation of the *D* value by about 50−70%. Accordingly, the values in Table 2 were also scaled by 2/3, which brought them closer

(55) Neese, F. *J. Chem. Phys.* **2005**, *122*, 034107-1−034107-13.
(56) ter Heerdt, P.; Stefan, M.; Goovaerts, E.; Canenschi, A.; Cornia, A. *J. Magn. Reson.* **2006**, *179*, 29−37.

to the experimental values. Hence, the major problem in the present case appears to be the determination of a reliably accurate theoretical geometry without imposing the geometric constraints of the protein environment. This would require very demanding QM/MM calculations that are outside the scope of the present work; thus, given the rather moderate match between theoretical and experimental geometries, a mismatch between the calculated and the measured, relatively small, *D* values is expected.

The Superposition Model. Mn^{2+} ZFS tensors can be also predicted using the superposition model (SPM) proposed by Newman and Urban,[57] using the atomic coordinates of the first coordination shell and a number of empirical parameters. Recently, this model has been used to account for the *D* and *E* parameters of a few Mn^{2+} proteins, and a good agreement between the calculated and experimental values has been reported.[58] Hence, we have tested this model as well, using the atomic coordinates of the oxygen ligands of enolase (Zn^{2+}/Mn^{2+})−PhAH crystals (for details, see the Supporting Information). The geometry of sites I and II in molecules A and B of the dimer, although in general similar, exhibit variations in Mn−O distances of up to 0.1 Å along with small changes in bond orientations, which are within experimental error. These subtle changes led to significantly different *D* and *E* values for the Mn^{2+} in the same site in molecules A or B, as listed in Table 2. Interestingly, the differences for site II are smaller, although this is not obvious from the differences in distances and orientations, and in this case, probably one can just take an average of the two. The average value, 32 mT, is 30% lower than the experimental value, and *E*/*D* is close to the experimental value. The sign of *D* is negative, as predicted by the DFT calculations for site II. In the case of site I, the difference between the values obtained for molecules A and B is large and involves a sign change, and therefore, we will not discuss it any further.

The orientation of the *z* axis of the SPM-calculated **D** of site II does not coincide with any of the Mn−O bond directions in both molecules A and B. For molecule A, *x* is 24° off of the Mn−O(W1002) direction, while for molecule B, the *y* axis is off the Ser539−Mn−PhAH axis by about 30°.

The subtle differences between the binding sites in molecules A and B, which could be within the experimental error of the crystallographic data, raises the issue of the effect of this error. Considering the relatively high resolution of the crystal structure, 1.54 Å, and that the accuracy of the protein crystallographic data is unlikely to reach that of small molecules, from this model, it seems that variations of up to 100% in the *D* and *E* values are expected just on the basis of the error in the coordinates for *D* values on the order of those found for enolase.

Conclusions

The structure of the enolase (Zn^{2+}/Mn^{2+})−PhAH complex has been solved to 1.54 Å resolution using X-ray crystallography, showing that the replacement of the native Mg^{2+} ions with Mn^{2+}/Zn^{2+} introduces only minor atom displacements in the binding site. The ZFS tensors of Mn^{2+} in the catalytic binding sites I and II were determined using single-crystal W-band EPR and ENDOR. Although Zn^{2+} was introduced to the crystal growth solution first and was, therefore, expected to primarily occupy site I, the EPR measurements resolved two metal sites with chemically inequivalent Mn^{2+}, showing that the higher affinity of Mn^{2+} to site I leads to site exchange, occurring either during crystal growth or later. The ^{1}H ENDOR spectra of the Mn^{2+} with the larger *D* value allowed its assignment to site I. These measurements also gave coordinates of protons of the water ligands of site I and of one of the water ligands of site II. Their involvement in a hydrogen-bond network, stabilizing the binding of PhAH, was illustrated as well. DFT calculations carried out on a cluster representing the catalytic site, with Mn^{2+} in site I and Zn^{2+} in site II, and vice versa, gave overestimated *D* values on the order of magnitude of those obtained experimentally. While the sign of *D* could not be determined experimentally, the sign of *D* for Mn^{2+} occupying site II was predicted to be negative. The sign of *D* remained ambiguous for the calculations with Mn^{2+} occupying site I since the calculated *E*/*D* values were close to the rhombic limit. Nevertheless, the larger *D* value was found for site II in the calculations, which disagrees with the experimental assignment. Apart from the trivial possibility that the error is inherent in the employed methodology, the discrepancy may well be due to small but significant differences between the optimized structures and the crystal structure. Although a reasonably large model of the active site was used (81 atoms), such differences have been observed for the fully optimized structures and were, only to a limited extent, resolved by adding geometric constraints to the optimization. Owing to the lack of a strong geometric preference for either Zn^{2+} or Mn^{2+}, such floppy active sites call for a QM/MM approach in order to obtain more accurate theoretical structures that properly reflect the constraints of the protein environment. Finally, both the experimental results and the DFT calculations showed that the principal axis system of the ZFS does not align with any of the Mn−ligand directions. For site I, the deviations were the smallest and were similar for the experimental tensor and the DFT calculated tensor obtained from the X-ray structure.

Acknowledgment. This research was supported by the DFG Schwerpunkt program "High field EPR in Physics, Chemistry and Biology" by the German−Israel Foundation for Scientific Research (D.G. and F.N.), by the The Ilse Katz Institute for Material Sciences and Magnetic Resonance Research (D.G.), and by NIH Grant GM 35752 (G.H.R.). We also thank Dr. A. Gilboa (Kalb) for helpful discussions. D.G. holds the Erich Klieger Chair of Chemical Physics. S.Z. gratefully acknowledges a postdoctoral fellowship from the Alexander von Humboldt Foundation.

Supporting Information Available: Description of the procedure used to determine the Euler angles relating the morphology and crystal axis systems and of the expressions of the superposition model used for calculating **D**. This material is available free of charge via the Internet at http://pubs.acs.org.

JA066124E

(57) Newman, D. J.; Urban, W. *Adv. Phys.* **1975**, *24*, 793−844.
(58) Tabares, L. C.; Cortez, N.; Agalidis, I.; Un, S. *J. Am. Chem. Soc*. **2005**, *127*, 6039−6047.